

Article

Corrosion Degradation Behaviors of Ti6Al4V Alloys in Simulated Marine Environments

Wei Chen ^{1,†}, Dalu Zhang ^{1,†}, Enlei Wang ^{1,*}, Feng Yan ¹, Lin Xiang ² and Zhiwen Xie ^{1,*}

¹ School of Mechanical Engineering and Automation, University of Science and Technology Liaoning, Anshan 114051, China; cwustl@126.com (W.C.); godroad7@163.com (D.Z.); yf65@sina.com (F.Y.)

² Precision Forming Center, Southwest Technology and Engineering Research Institute, Chongqing 400039, China; xlin0731@163.com

* Correspondence: enleiwang@ustl.edu.cn (E.W.); xzwustl@126.com (Z.X.)

† These authors contributed equally to this work.

Abstract: Detailed tests and characterizations were used to investigate the corrosion degradation behaviors of Ti6Al4V alloys in simulated marine environments. These alloys suffered from very slight pitting and a miniscule weight loss of 0.018 mg/cm² during the 50 cycle salt spray exposure but experienced significant oxygen erosion in the high-temperature oxidation test, resulting in a high weight gain of 2.657 mg/cm² at 400 h. The oxidation and degradation reactions simultaneously occurred during the high-temperature hot salt test. The chlorine (Cl₂) induced by the eutectic reaction of the mixed salts accelerated the degradation of the substrate and led to a higher weight gain of 4.265 mg/cm² at 400 h. In contrast, this alloy suffered from severe corrosion damage during the high-temperature hot salt–water vapor synergy test. The degradation of TiO₂, Al₂O₃, and V₂O₅ was aggravated by the synergistic action of chlorine salt and water. The reaction forming hydrochloric acid (HCl) further degraded the matrix metal and consequently led to a high weight loss of 16.358 mg/cm² at 400 h. These current findings provide a comprehensive understanding for the degradation mechanisms of Ti alloys in these specific marine environments.



Citation: Chen, W.; Zhang, D.; Wang, E.; Yan, F.; Xiang, L.; Xie, Z. Corrosion Degradation Behaviors of Ti6Al4V Alloys in Simulated Marine Environments. *Coatings* **2022**, *12*, 1028. <https://doi.org/10.3390/coatings12071028>

Academic Editor: Claudio Mele

Received: 24 May 2022

Accepted: 17 July 2022

Published: 20 July 2022

Publisher's Note: MDPI stays neutral with regard to jurisdictional claims in published maps and institutional affiliations.



Copyright: © 2022 by the authors. Licensee MDPI, Basel, Switzerland. This article is an open access article distributed under the terms and conditions of the Creative Commons Attribution (CC BY) license (<https://creativecommons.org/licenses/by/4.0/>).

Keywords: Ti6Al4V alloy; salt spray; oxidation; hot salt test; hot salt–water vapor test

1. Introduction

Ti6Al4V alloy is characterized by its light weight, high specific strength, non-magnetic properties, and good biocompatibility [1,2]. Currently, it is widely used in the fields of national defense; the biomedical and marine industries; and aerospace, especially in the manufacture of aero–engine hot-end components (such as compressor blades, etc.), where the lightweight Ti6Al4V alloy has shown great potential for engineering applications [3–9]. However, the literature has reported that these Ti alloy components experienced prominent oxidation erosion during high-temperature air exposure [10–13]. In addition, the literature reported that these components also suffered from severe simultaneous oxidation and degradation reactions during marine environment exposure (e.g., hot salt or hot salt–water vapor) [14–18]. The strong synergistic damage of the oxidation and degradation reactions greatly threatens the long-term service life of these hot end components. Therefore, it is necessary to clarify the corrosion degradation behaviors and mechanisms of Ti alloy components during this specific marine environment exposure.

The oxidation and corrosion behaviors of Ti alloy components are the current research focus in the field of corrosion and protection [19–23]. For example, Bower. K et al. [20] reported that the mass of this alloy hardly changed after approximately 400 h salt spray exposure, but a TiO₂ layer grew on the surface of this alloy. Meanwhile, a significant oxygen-rich layer appeared beneath the oxide layer and caused the embrittlement and property degradation of this alloy. Aca et al. [13] investigated the oxidation behavior of the Ti alloy at 500–600 °C. They found that TiO₂ and Al₂O₃ were the main constituent phases of the oxide

layer. Dai et al. [24] reported that the Cl_2 product formed during the hot salt corrosion test of the Ti2AlNb alloy, which further reacted with the substrate to produce volatile chlorides that resulted in severe cracking of the oxide layer. Wang et al. [14] investigated the oxidation behavior of Ti6Al4V in water vapor at 600–800 °C. The results show that the surface of the sample appeared to be dominated by alumina and rutile phases, and the hardness increased significantly with the increasing temperature.

Apparently, the damage failure characteristics of the Ti alloys in different marine environments are very different. In addition, the oxidative erosion and degradation reactions show a significant effect on their corrosion resistance during the marine environment exposure. Although these current results provided feasible explanations for the corrosion failure behaviors of Ti alloys in different marine environments, these degradation mechanisms are still expected to be further strengthened in the upcoming investigations. In this study, a detailed comparison of the corrosion degradation behaviors of Ti6Al4V alloys in different environments was described by the oxidation, salt spray, hot salt, and hot salt–water vapor synergy tests; the potential corrosion mechanism will be discussed in detail.

2. Materials and Methods

The test material is Ti6Al4V alloy, which is a typical ($\alpha + \beta$) type alloy. The length, width, and thickness of this sample were 15 mm, 15 mm, and 5 mm (see Figure 1), respectively. The individual elemental contents of the original samples are shown in Table 1.

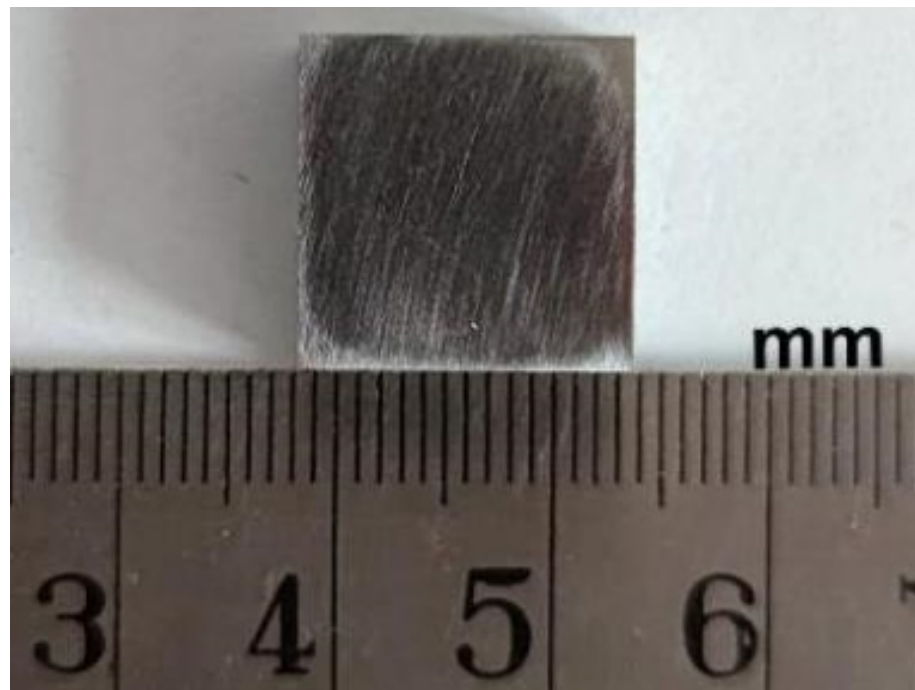


Figure 1. Optical morphology of Ti6Al4V alloy sample.

Table 1. Chemical composition of the original sample (weight percentage).

Al	V	Fe	C	O	N	Ti
5.5–6.8	3.5–4.5	≤0.3	≤0.1	≤0.2	≤0.05	Bal.

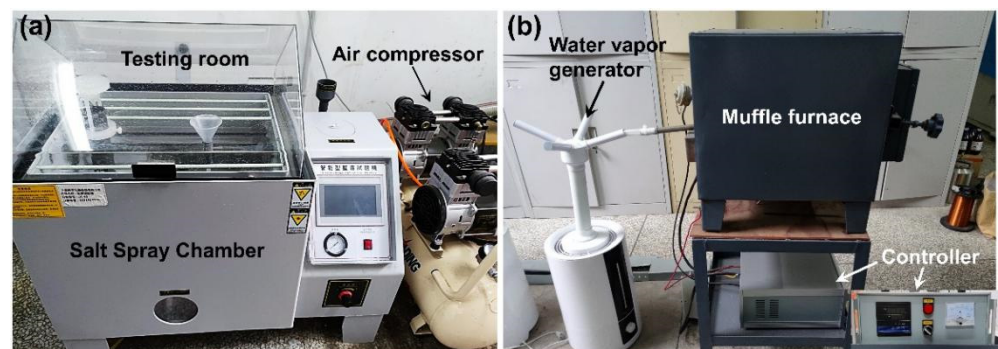
These samples were sanded by using 320 grit and 600 grit SiC sandpapers and then cleaned by ultrasonic in ethanol solution for 20 min. The specific experimental design is shown in Table 2.

Table 2. Details of the test design for Ti6Al4V alloy.

Sample	Test Type	Time
H0	Untested sample	-
H1	Salt spray test	50 cycles
H2	High-temperature oxidation test	400 h
H3	High-temperature hot salt test	400 h
H4	High-temperature hot salt–water vapor synergy test	400 h

As shown in Figure 2a, the salt spray test was conducted in a salt spray tester (JK-60, Shanghai Meiyu Instruments Co., Shanghai, China). The test was set to a cycle of 24 h for 50 cycles. The solution in the salt spray chamber was a mixed salt solution with a concentration of $5\% \pm 0.1\%$ configured from 25 wt.% NaCl + 75 wt.% Na₂SO₄. The pH value of this solution was adjusted to 4 with sulfuric acid. The ambient temperature in the test chamber was set to 35 ± 2 °C, and the spray preheating temperature was 46 °C. The atomization conditions were based on 0.28 m³ space to atomize 2.8 L of solution in 24 h, and the settling rate was adjusted to 1–3 mL/(80 cm²·h). The pH value of this salt solution was measured once every 24 h.

High-temperature oxidation and high-temperature hot salt tests were performed in a muffle furnace. The hot salt–water vapor synergy test was completed in a muffle furnace equipped with a water vapor generator (see Figure 2b). Firstly, a salt mixture of 75 wt.% Na₂SO₄ + 25 wt.% NaCl was coated on the samples that were used for hot salt corrosion and hot salt–water vapor tests. To ensure the uniformity of the salt film on the coating's surface, these salt application processes were performed several times to ensure that the salt content of the sample was 3–5 mg/cm². The test temperatures and heating rates of these above tests were 650 °C and 10 °C/min, respectively. The test duration time was 400 h. These samples were taken and weighed every 20 h, and the mass changes of these tested samples were weighed by an electronic balance with an accuracy of 0.0001 g. In order to reduce the experimental variation error, all samples were measured with three sets of parallel specimens, and the average mass was taken as the final result.

**Figure 2.** (a) Salt spray test equipment; (b) hot salt–water vapor test equipment.

The crystal structures of all corroded samples were characterized by the X-ray diffraction (XRD, X' Pert Powder, PANalytical B.V., Almelo, Netherlands) with a Cu-K α radiation source, a scanning range of 20°–90°, and a scanning time of 2 min. X-ray photoelectron spectrometer (XPS, ESCALAB 250Xi, ThermoFisher, K-Alpha+, Waltham, MA, USA) with an Al-K α emission source was used to analyze the elemental chemical valence state of the sample surface. The C 1s peak of 284.8 eV was used as the charge calibration peak for the calibration of the spectrum. The surface and cross-sectional images of all corroded samples were characterized by scanning electron microscopy (SEM, Zeiss Σ IGMA HD, Carl Zeiss, Jena, Germany). The local elemental compositions and distributions of all corroded samples were determined by energy dispersive spectroscopy (EDS).

3. Results

Figure 3 displays the corrosion kinetic curves of all tested samples. As shown in Figure 3a, sample H1 exhibits a relatively stable weight variation trend during the whole salt spray environment exposure, and a tiny weight loss of 0.018 mg/cm^2 is identified after the 50 day test, indicating good corrosion resistance. As shown in Figure 3b, sample H2 exhibits an approximately linear weight gain trend, and a weight gain value of 2.657 mg/cm^2 is characterized after a 400 h oxidation test. In comparison, sample H3 showed a parabolic weight gain trend during the hot salt test but also possesses a higher gain value of 4.265 mg/cm^2 at 400 h, indicating a more severe oxidation erosion reaction. However, sample H4 experiences a slight weight gain during the initial stage but suffers from a severe weight loss with the increase of the test time. A high weight loss value of 16.358 mg/cm^2 clearly confirms that a significant corrosion degradation occurs in the hot salt–water vapor synergy environment.

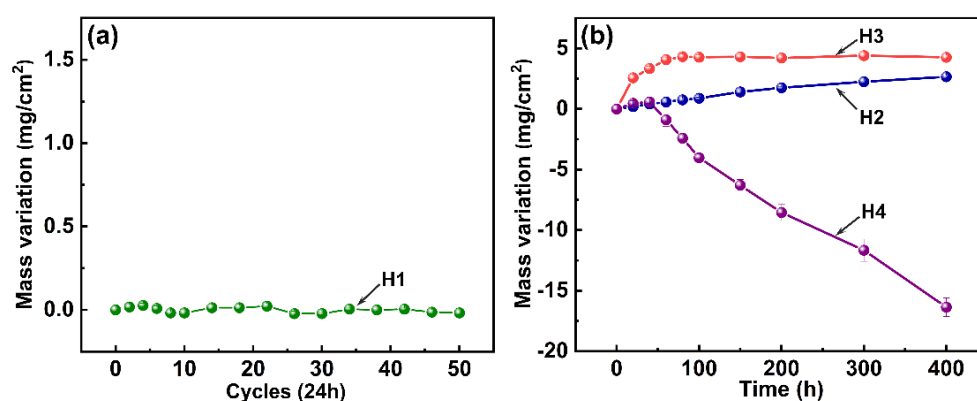


Figure 3. Corrosion kinetic curves of all tested samples: (a) H1; (b) H2, H3, H4.

Figure 4 shows the macroscopic morphologies of all tested samples. The untested sample in Figure 4a has a bright metallic luster accompanied by numerous grooves induced by surface treatment. As shown in Figure 4b, these grooves are also observed on the surface of sample H1, but the metallic luster disappears and some visible black spots appear on the surface of this sample, indicating that a slight pit corrosion occurs during the salt spray environment exposure. Sample H2 presents a densely earthy yellow surface after the oxidation test; as shown in Figure 4c, this morphology is accordance with typical titanium oxide [13]. In contrast, sample H3 has a bright yellow surface accompanied by a thicker oxide layer; as shown in Figure 4d, the visible oxide layer cracking occurs at the edge of this sample, indicating an accelerated oxidation reaction during the hot salt exposure. As shown in Figure 4e, this yellow oxide layer almost completely degrades, while a black surface with numerous uneven corrosion pits is observed on the surface of sample H4, proving that a significant degradation reaction occurs during the hot salt–water vapor synergy exposure.

Figure 5a shows the XRD (X-ray diffraction) patterns of all tested samples. These diffraction peaks of sample H1 are mainly attributed to the initial α -Ti and $(\alpha + \beta)$ -Ti phases. It has been reported that a passivation film consisting mainly of TiO_2 forms on the surface of the titanium alloy during the salt spray exposure [20,25]. As shown in Figure 5c, the $\text{Ti}2p_{3/2}$ and $\text{Ti}2p_{1/2}$ peaks in sample H1 locate at 458.48 and 464.17 eV, respectively, which correspond to the Ti–O binding state, confirming the formation of a thin TiO_2 passivation film [26]. Sample H2 is mainly composed of the TiO_2 and Al_2O_3 phases, indicating a prominent oxidation reaction during the high-temperature air exposure. Sample H3 shows a phase composition similar to that of sample H2, and these visible TiO_2 and Al_2O_3 phases are identified in its XRD pattern. According to the two peaks deconvoluted from the O1s spectrum in Figure 5d, it can be determined that the oxides on the surface of sample H3 are TiO_2 and Al_2O_3 [27]. Sample H4 is mainly composed of the TiO_2 , Al_2O_3 , and AlTi_3

phases, but the intensity of these TiO_2 and Al_2O_3 peaks obviously weakens. In combination with Figure 5b, a significant color change can be seen in the deionized water for cleaning sample H4, and the color of deionized water is obviously darker with the increase of test time, indicating an aggravated degradation reaction occurs during the hot salt–water vapor synergy exposure.

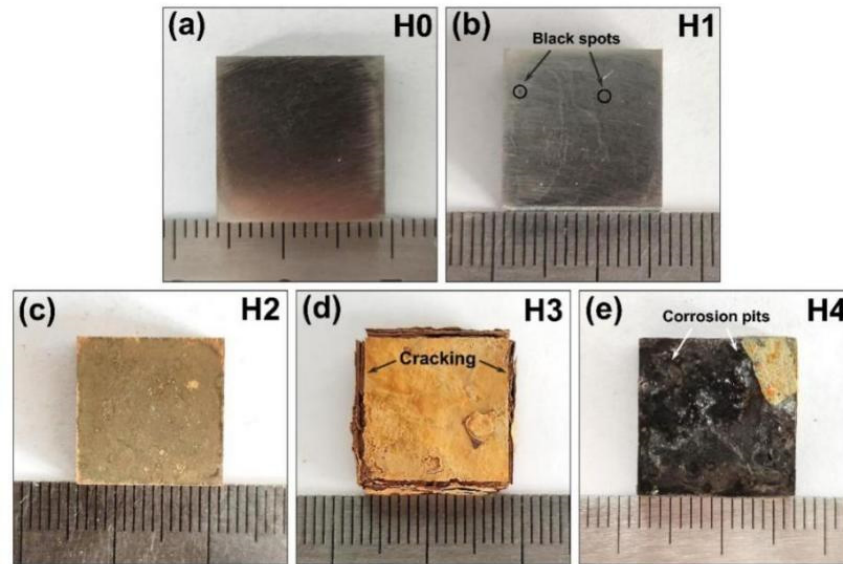


Figure 4. Macroscopic morphologies of all tested samples: (a) H0; (b) H1; (c) H2; (d) H3; and (e) H4.

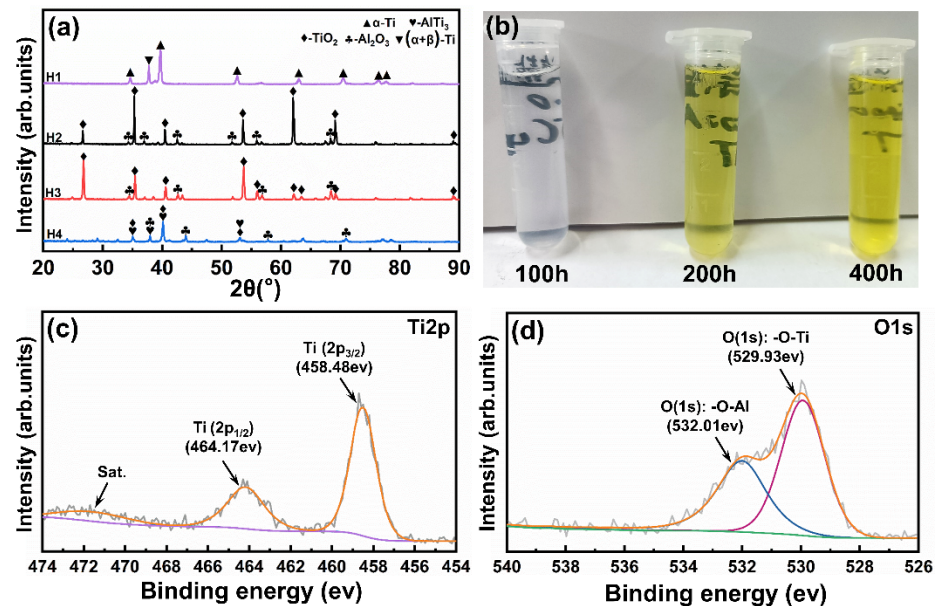


Figure 5. (a) XRD patterns of all tested samples; (b) color change of deionized water after washing of sample H4; (c) Ti2p spectrum of sample H1; and (d) O1s spectrum of sample H3.

Figure 6 displays the surface and cross-sectional SEM images and EDS spectra of sample H1. As presented in Figure 6a, sample H1 shows initial surface morphology accompanied by numerous parallel grooves. However, some visible pits also appear on its surface, indicating slight corrosion degradation during the salt spray exposure. Figure 6b,c show the cross-sectional SEM images and elemental mappings of sample H1 after the salt spray test. It can be found that sample H1 retains its structure, without visible damage or degradation products, indicating a considerable resistance to salt spray corrosion.

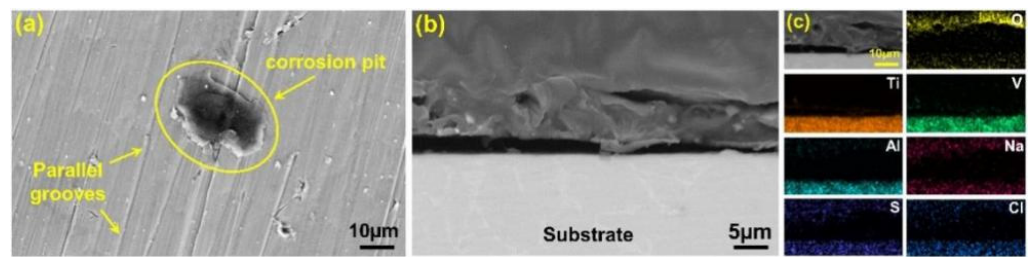


Figure 6. Surface SEM images (a), cross-sectional SEM image (b), and elemental mappings (c) of sample H1.

Figure 7a shows the SEM surface images of sample H2 after the oxidation test. A relatively dense and coarse surface feature is characterized in sample H2. The local enlarged image in Figure 7d shows that numerous long strip fibers distribute on the surface of this sample; as determined by the XRD result of Figure 5, these fibrous products are accordance with the growth morphology of typical TiO_2 phases [13]. In contrast, sample H3 shows a loose surface morphology after the hot salt test; as shown in Figure 7b, plenty of micro-pores appear on the surface of this sample, indicating the occurrence of a potential corrosion degradation reaction. The local enlarged image in Figure 7e shows that these degradation products are predominantly stacked in short rods and granular structures, and a number of visible pores are clearly observed in the sample. In contrast to sample H3, sample H4 suffers from more serious corrosion damage during the hot salt–water vapor test; as shown in Figure 7c, a loosely granular surface accompanied by numerous deep holes is clearly observed in this sample. The local enlarged image in Figure 7f further reveals that the surface of sample H4 is characterize by a loosely honeycomb-like structure, without strip fiber, indicating that a significant degradation reaction occurs during hot salt–water vapor exposure.

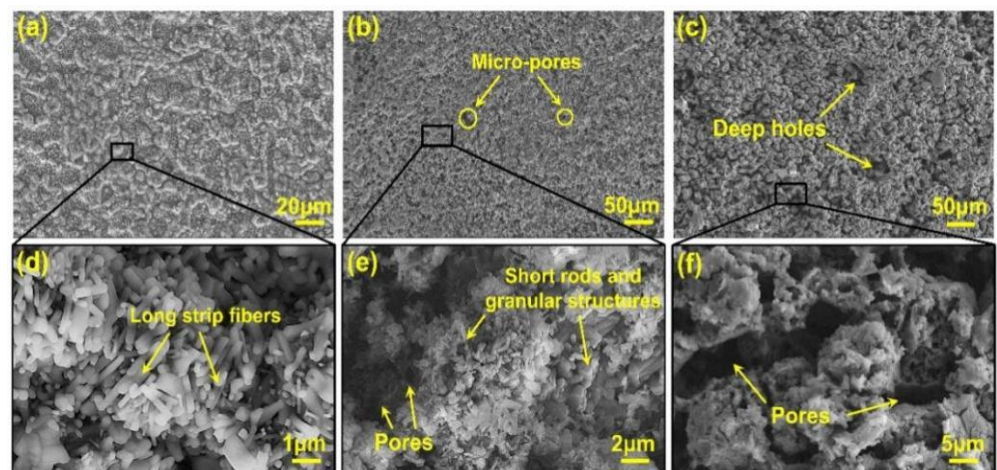


Figure 7. Surface SEM images of the tested samples: (a) and (d) H2; (b) and (e) H3; and (c) and (f) H4.

Figure 8 shows the cross-sectional SEM images and element mappings of samples H2, H3, and H4. As shown in Figure 8a,b, a relatively uniform oxide layer with a thickness of $30\ \mu\text{m}$ forms on the surface of sample H2 during the oxidation test, and some slight crackings also distribute the corresponding enrichment zones of alumina. In contrast, sample H3 experiences an accelerated oxidation reaction during the hot salt test; as shown in Figure 8c, the thickness value of the oxidation layer in sample H3 is up to $830\ \mu\text{m}$, which is much higher than in sample H2. Moreover, the oxidation layer of sample H3 suffers from a severe fracture accompanied by some visible layered crackings. The element mappings in Figure 8d reveal that some enrichment layers of alumina appear in the fracture zones of this oxide layer, indicating a strong correlation between Al enrichment and layered fractures.

As shown in Figure 8e,f, this oxide layer hardly appears on the surface of sample H4, but a large number of corrosion holes form in the substrate matrix, both of which indicate that a severe corrosion degradation reaction occurs during the hot salt–water vapor test.

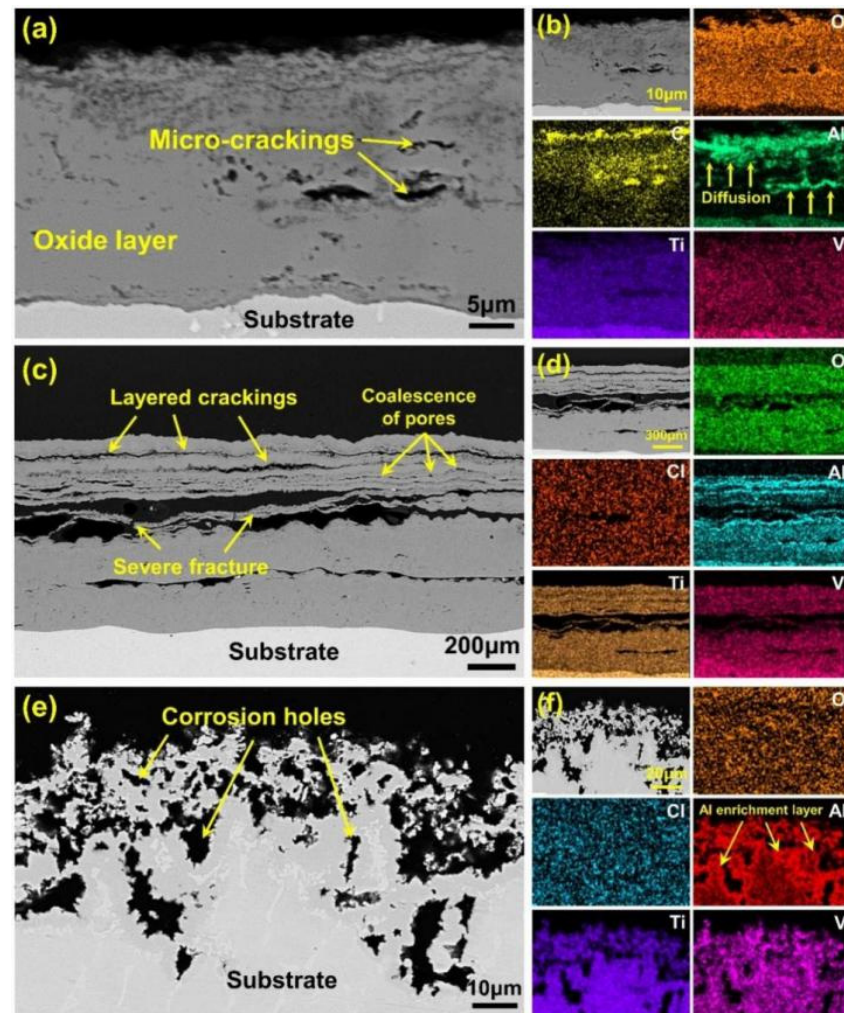


Figure 8. Cross-sectional SEM images and element mappings of the tested samples: (a) and (b) H2; (c) and (d) H3; and (e) and (f) H4.

4. Discussion

Apparently, Ti6Al4V alloys are very sensitive to these service environments. Reasonable explanations for the damage mechanisms of Ti6Al4V alloys in evaluated environments are illustrated in Figure 9. As determined by the XRD, XPS, and SEM results, sample H1 shows considerable corrosion resistance during the salt spray environment exposure, which is likely attributed to the formation of a passivation film [7,28]. As displayed in Figure 9a, it has been reported that the standard potential of the 4s electron layer of the Ti6Al4V alloy is very small, and it is relatively easy to lose electrons. Therefore, a passivation film consisting of TiO₂ rapidly forms on the substrate according to the reaction Equation (1).



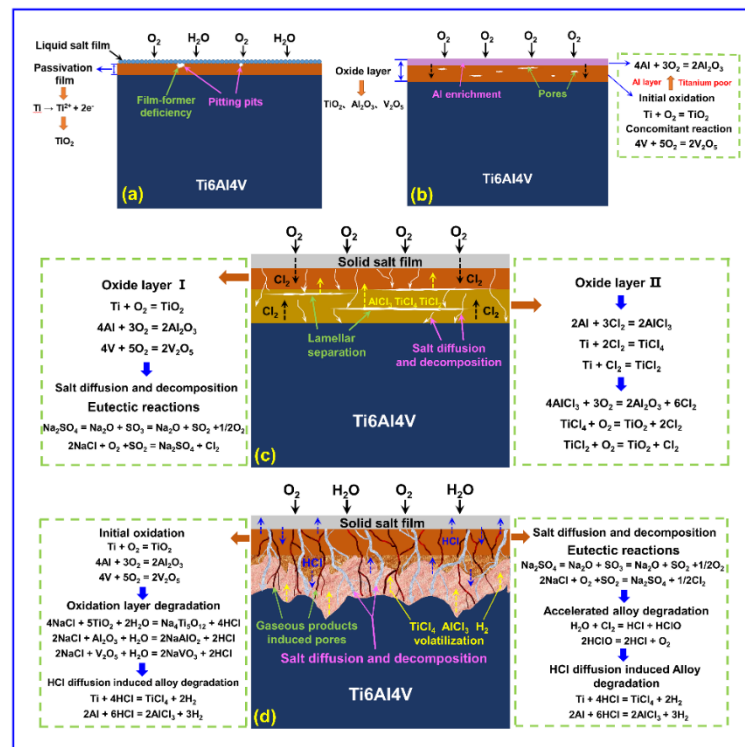


Figure 9. Corrosion damage mechanism diagrams of all tested samples: (a) salt spray; (b) oxidation; (c) hot salt corrosion; and (d) hot salt–water vapor synergy.

Although the passivation film is only a few nanometers or tens of nanometers thick, it has a very dense structure with good anti-corrosion properties in salt spray conditions. Unfortunately, the growth of this passivation film tends to be unsustainable as these forming agents (e.g., OH^- and O_2) are not sufficient, which eventually leads to slight local pitting [29,30].

Sample H2 exhibits consistent weight gain during the oxidation test, which may have been caused by the prominent oxidation reaction. As shown in Figure 9b, a severe oxidation reaction occurred in the initial stages. It has been reported that the binding capacity of Ti to O_2 is greater than that of Al and V [31], and thus the Ti atom firstly reacts with O_2 to form TiO_2 according to Equation (2).



The continuous reaction leads to the decrease of Ti in the surface layer of the substrate and the depletion of Ti at the interface between the oxide layer and substrate. The change of element partial pressure leads to the rapid diffusion of Al in TiO_2 and enrichment outside the oxide layer [32], forming an Al-rich region and an Al_2O_3 layer according to Equation (3). Meanwhile, the V further reacts with the O_2 to form V_2O_5 according to Equation (4). However, the content of V is so small, and no significant diffraction peaks of V_2O_5 are detected in the XRD.



The O_2 continues to react with the substrate through the oxide layer, resulting in the growth of a thick oxide layer [33,34]. However, the diffusion capacity of the O_2 penetrating into the interior of the substrate gradually decreases with the increase of the oxide layer thickness, which is responsible for the gradual decrease in slope of the kinetic curve of the sample H2 (see Figure 1b).

Compared with sample H2, sample H3 suffers from an aggravated erosion and delamination failure during the hot salt corrosion test, which mainly originated from the

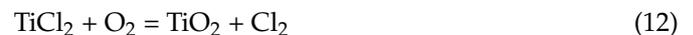
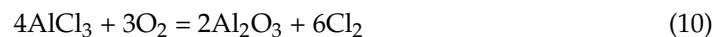
accelerated oxidation reaction process. As shown in Figure 9c, an original oxide layer consisting of the TiO_2 , Al_2O_3 , and V_2O_5 forms on the substrate surface according to Equations (2)–(4). Some studies have reported that the salt mixture hardly reacts with these oxidation products at $650\text{ }^\circ\text{C}$ but possesses a melting point of $645\text{ }^\circ\text{C}$. Therefore, this molten salt mixture diffuses internally through the oxide layer and further undergoes eutectic reactions obeying Equations (5) and (6) [4,21].



Subsequently, the Cl_2 further reacts with Ti and Al to form volatile chlorides (e.g., AlCl_3 , TiCl_4 , and TiCl_2) according to Equations (7)–(9), triggering a rapid degradation of the substrate matrix and the production of a large number of micro-pores [35].

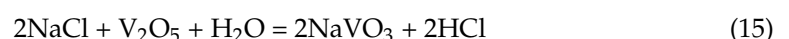
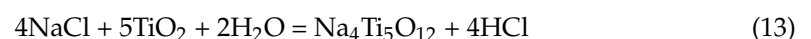


Moreover, these volatile products further react with the O_2 to produce TiO_2 , Al_2O_3 , V_2O_5 , and Cl_2 , according to Equations (10)–(12). As identified by SEM image of Figure 6b, these reactions between the gaseous products ultimately result in a loose and porous surface morphology.



Obviously, the Cl_2 acts as a key carrier, accelerating the degradation reaction of the substrate, and results in the rapid growth of the oxide layer. As identified by the SEM image of Figure 8c, the continuous volatilization of chloride and the significant structure differences of these oxides trigger high thermomechanical growth stress, which eventually results in a severe layered separation and local cracking [36] since the coefficients of thermal expansion of TiO_2 , Al_2O_3 , and Ti6Al4V alloy are 8.2×10^{-6} , 8.1×10^{-6} , and $10\text{--}12 \times 10^{-6}\text{ K}^{-1}$, respectively [25]. Therefore, the significant difference in thermal expansion coefficients between the oxide layer and substrate eventually induces the initiation of surface ring breaking [37]. Moreover, the visible fracture of this oxide layer further accelerates the penetration of the O_2 and results in the rapid growth of a new oxide layer.

Sample H4 experiences aggravated weight loss during the hot salt–water vapor synergy exposure, which mainly originates from a prominent degradation reaction. In the initial stages of this test, the oxidation of the Ti6Al4V alloy dominates the reaction. As presented in Figure 9d, an initial composite oxide layer consisting of TiO_2 , Al_2O_3 , and V_2O_5 rapidly forms on the substrate surface obeying Equations (2)–(4) [38,39]. The Cl_2 produced by the eutectic reaction between the mixed salts diffuses in both directions near the oxide layer, and some of the Cl_2 enters the interior of the oxide layer to react with Ti and Al to produce volatile gaseous chloride, which induces the appearance and growth of pores obeying Equations (7)–(9). Meanwhile, the synergistic effect of high-temperature water vapor triggers severe erosive degradation of the surface oxide layer. The degradation reactions of these oxides occur according to Equations (13)–(15), leading to the severe consumption of these oxides and the formation of HCl products [36,39].



Subsequently, according to Equations (16) and (17), the hydrochloric acid penetrates the loose oxide layer and further reacts with the matrix metal to form volatile chlorides and H₂.



Additionally, the oxide layer is severely damaged and eroded by the synergistic action of Cl₂ and high-temperature hot salt–water vapor, which results in the downward diffusion of salt mixture. The mixed salt in the molten state further diffuses into the matrix metal, triggering the formation of Cl₂ due to the eutectic reaction. The Cl₂ reacts with H₂O to produce HCl according to Equations (18) and (19). Moreover, the HCl reacts with the matrix metal to form volatile chlorides [40].



In summary, the water vapor triggers a significant corrosion reaction during the hot salt–water vapor synergy test, which accelerates the degradation process of both these oxides and matrix metals, resulting in the appearance of numerous corrosion pores. Meanwhile, the formation of volatile chlorides and gas products further leads to a severe weight loss of sample H4.

5. Conclusions

This study investigated the corrosion degradation behaviors of Ti6Al4V alloys in simulated marine environments. This alloy showed good corrosion resistance and a tiny weight loss of 0.018 mg/cm² during the 50 cycle salt spray due to the formation of a passivation film consisting of TiO₂. However, this alloy suffered from a prominent oxidation erosion reaction during the high-temperature oxidation test, leading to the formation of a dense (TiO₂ + Al₂O₃ + V₂O₅) layer and a high weight gain value of 2.657 mg/cm² at 400 h. In contrast, this alloy suffered from simultaneous oxidation erosion and a degradation reaction during the high-temperature hot salt test. The Cl₂ produced by the mixed salt eutectic reaction accelerated the degradation of the substrate, triggering the formation of volatile chlorides (e.g., AlCl₃ and TiCl₄). These chlorides further reacted with oxygen to form loose oxides (e.g., TiO₂ and Al₂O₃) and consequently resulted in a higher weight gain of 4.265 mg/cm² at 400 h. During the high-temperature hot salt–water vapor test, this alloy suffered from severe corrosion degradation due to the strong synergism of chloride salt and water vapor. The reaction between chloride salt, water, and oxide induced a rapid degradation of these mixed oxides (TiO₂ + Al₂O₃ + V₂O₅). The reaction forming HCl aggravated the corrosion degradation of the substrate. The overflow of these chlorides eventually resulted in a severe weight loss of −16.358 mg/cm² at 400 h.

Author Contributions: Conceptualization, E.W. and Z.X.; methodology, F.Y.; investigation, W.C. and D.Z.; and supervision, L.X. All authors have read and agreed to the published version of the manuscript.

Funding: This study was supported by the University of Science and Technology Liaoning Talent Project Grants (601011507-07) and the Southwest Institute of Technology and Engineering Cooperation fund (HDHDW5902020103).

Institutional Review Board Statement: Not applicable.

Informed Consent Statement: Not applicable.

Data Availability Statement: No new data were created or analyzed in this study. Data sharing is not applicable to this article.

Conflicts of Interest: The authors declare no conflict of interest.

References

1. Banerjee, D.; Williams, J.C. Perspectives on Titanium Science and Technology. *Acta Mater.* **2013**, *61*, 844–879. [[CrossRef](#)]
2. Zabler, S. Interstitial Oxygen diffusion hardening—A practical route for the surface protection of titanium. *Mater. Charact.* **2011**, *62*, 1205–1213. [[CrossRef](#)]
3. Khan, M.A.; Sundarajan, S.; Natarajan, S.; Parameswaran, P.; Mohandas, E. Oxidation and Hot Corrosion Behavior of Nickel-Based Superalloy for Gas Turbine Applications. *Mater. Manuf. Process.* **2014**, *29*, 832–839. [[CrossRef](#)]
4. Mitoraj-Królikowska, M.; Godlewska, E. Hot corrosion behaviour of ($\gamma+\alpha$ 2)-Ti-46Al-8Nb (at.%) and α -Ti-6Al-1Mn (at.%) alloys. *Corros. Sci.* **2017**, *115*, 18–29. [[CrossRef](#)]
5. Boyer, R.R. An overview on the use of titanium in the aerospace industry. *Mater. Sci. Eng. A* **1996**, *213*, 103–114. [[CrossRef](#)]
6. Filip, R.; Kubiak, K.; Ziaja, W.; Sieniawski, J. The effect of microstructure on the mechanical properties of two-phase titanium alloys. *J. Mater. Process. Technol.* **2003**, *133*, 84–89. [[CrossRef](#)]
7. Cizak, C.; Popa, I.; Brossard, J.-M.; Monceau, D.; Chevalier, S. NaCl-Induced High-Temperature Corrosion of β 21S Ti Alloy. *Oxid. Met.* **2017**, *87*, 729–740. [[CrossRef](#)]
8. Keddam, M.; Taktak, S. Characterization and diffusion model for the titanium boride layers formed on the Ti6Al4V alloy by plasma paste boriding. *Appl. Surf. Sci.* **2017**, *399*, 229–236. [[CrossRef](#)]
9. Brice, D.; Samimi, P.; Ghamarian, I.; Liu, Y.; Brice, R.; Reidy, R.; Cotton, J.; Kaufman, M.; Collins, P. Oxidation behavior and microstructural decomposition of Ti-6Al-4V and Ti-6Al-4V-1B sheet. *Corros. Sci.* **2016**, *112*, 338–346. [[CrossRef](#)]
10. Guleryuz, H.; Cimenoglu, H. Oxidation of Ti-6Al-4V alloy. *J. Alloys Compd.* **2009**, *472*, 241–246. [[CrossRef](#)]
11. Wang, X.; Li, C.; Li, M.; Cao, J. Enhancing high-temperature oxidation resistance of Ti6Al4V alloy by simple surface aluminization. *Corros. Sci.* **2021**, *192*, 109810. [[CrossRef](#)]
12. Kumar, S.; Narayanan, T.S.; Raman, S.G.S.; Seshadri, S. Thermal oxidation of Ti6Al4V alloy: Microstructural and electrochemical characterization. *Mater. Chem. Phys.* **2010**, *119*, 337–346. [[CrossRef](#)]
13. Casadebaigt, A.; Hugues, J.; Monceau, D. High temperature oxidation and embrittlement at 500–600 °C of Ti-6Al-4V alloy fabricated by Laser and Electron Beam Melting. *Corros. Sci.* **2020**, *175*, 108875. [[CrossRef](#)]
14. Wang, S.; Liao, Z.; Liu, Y.; Liu, W. Influence of thermal oxidation temperature on the microstructural and tribological behavior of Ti6Al4V alloy. *Surf. Coat. Technol.* **2014**, *240*, 470–477. [[CrossRef](#)]
15. Kumar, S.; Chattopadhyay, K.; Mahobia, G.; Singh, V. Hot corrosion behaviour of Ti-6Al-4V modified by ultrasonic shot peening. *Mater. Des.* **2016**, *110*, 196–206. [[CrossRef](#)]
16. Anuwar, M.; Jayaganthan, R.; Tewari, V.; Arivazhagan, N. A study on the hot corrosion behavior of Ti-6Al-4V alloy. *Mater. Lett.* **2007**, *61*, 1483–1488. [[CrossRef](#)]
17. Jamesh, M.; Kumar, S.; Narayanan, T.S.N.S.; Chu, P.K. Effect of thermal oxidation on the corrosion resistance of Ti6Al4V alloy in hydrochloric and nitric acid medium. *Mater. Corros.* **2012**, *64*, 902–907. [[CrossRef](#)]
18. Shao, L.; Xie, G.; Liu, X.; Wu, Y.; Yu, J.; Hao, Z.; Lu, W.; Liu, X. Combustion behaviour and mechanism of TC4 and TC11 alloys. *Corros. Sci.* **2020**, *168*, 108564. [[CrossRef](#)]
19. Chellaganesh, D.; Khan, M.A.; Jappes, J.T.W. Hot corrosion behaviour of nickel-iron-based superalloy in gas turbine application. *Int. J. Ambient Energy* **2018**, *41*, 901–905. [[CrossRef](#)]
20. Bower, K.; Murray, S.; Reinhart, A.; Nieto, A. Corrosion resistance of selective laser melted Ti-6Al-4V alloy in salt fog environment. *Results Mater.* **2020**, *8*, 100122. [[CrossRef](#)]
21. Omoniyi, P.; Akinlabi, E.; Mahamood, R.; Jen, T. Corrosion resistance of heat treated Ti6Al4V in NaCl. *Chem. Data Collect.* **2021**, *36*, 100780. [[CrossRef](#)]
22. Dai, J.; Zhu, J.; Chen, C.; Weng, F. High temperature oxidation behavior and research status of modifications on improving high temperature oxidation resistance of titanium alloys and titanium aluminides: A review. *J. Alloys Compd.* **2016**, *685*, 784–798. [[CrossRef](#)]
23. Kitashima, T.; Hara, T.; Yang, Y.; Hara, Y. Oxidation-nitridation-induced recrystallization in a near- α titanium alloy. *Mater. Des.* **2018**, *137*, 355–360. [[CrossRef](#)]
24. Dai, J.; Sun, C.; Wang, A.; Zhang, H.; Li, S.; Zhang, H. High temperature oxidation and hot corrosion behaviors of Ti2AlNb alloy at 923 K and 1023 K. *Corros. Sci.* **2021**, *184*, 109336. [[CrossRef](#)]
25. Aghion, E.; Guinguis, I.; Goldman, J. Corrosion Behavior of Nano/Sub-Micron F401 Titanium Alloy. *Adv. Eng. Mater.* **2014**, *17*, 626–631. [[CrossRef](#)]
26. Aas, N.; Pringle, T.J.; Bowker, M. Adsorption and decomposition of methanol on TiO₂, SrTiO₃ and SrO. *J. Chem. Soc. Faraday Trans.* **1994**, *90*, 1015–1022. [[CrossRef](#)]
27. Wu, L.-K.; Wu, J.-J.; Wu, W.-Y.; Yan, H.-J.; Jiang, M.-Y.; Cao, F.-H. Hot corrosion behavior of electrodeposited SiO₂ coating on TiAl alloy. *Corros. Sci.* **2020**, *174*, 108827. [[CrossRef](#)]
28. Hao, G.; Yao, Z.; Jiang, Z. Salt spray corrosion test of micro-plasma oxidation ceramic coatings on Ti alloy. *Rare Met.* **2007**, *26*, 560–564. [[CrossRef](#)]
29. Geng, M.; He, G.; Sun, Z.; Chen, J.; Yang, Z.; Li, Y. Corrosion Damage Mechanism of TiN/ZrN Nanoscale Multilayer Anti-Erosion Coating. *Coatings* **2018**, *8*, 400. [[CrossRef](#)]
30. Wu, B.; Pan, Z.; Li, S.; Cuiuri, D.; Ding, D.; Li, H. The anisotropic corrosion behaviour of wire arc additive manufactured Ti-6Al-4V alloy in 3.5% NaCl solution. *Corros. Sci.* **2018**, *137*, 176–183. [[CrossRef](#)]

31. Zhou, Y.; Zhang, Q.; Liu, J.; Cui, X.; Mo, J.; Wang, S. Wear characteristics of a thermally oxidized and vacuum diffusion heat treated coating on Ti-6Al-4V alloy. *Wear* **2015**, *344–345*, 9–21. [[CrossRef](#)]
32. Omidbakhsh, F.; Ebrahimi, A.; Mousavi, S.; Khosroshahi, R.; Nazarpour, S. Effect of oxygen boost diffusion treatment on fatigue behavior of Ti-4Al-2V alloy. *Surf. Coat. Technol.* **2011**, *205*, 2954–2963. [[CrossRef](#)]
33. Du, H.; Datta, P.; Lewis, D.; Burnell-Gray, J. Air oxidation behaviour of Ti6Al4V alloy between 650 and 850°. *Corros. Sci.* **1994**, *36*, 631–642. [[CrossRef](#)]
34. Liang, Z.; Tang, B.; Gui, Y.; Zhao, Q. High-Temperature Oxidation Behavior of the Ti-6Al-4V Alloy Manufactured by Selective Laser Sintering. *JOM* **2019**, *71*, 3600–3605. [[CrossRef](#)]
35. Pustode, M.D.; Chakraborty, P.; Padekar, B.S.; Shukla, S.; Raja, V.S. Hot Salt Stress Corrosion Cracking Study of Selective Laser Melted Ti-6Al-4V Alloy. *J. Mater. Eng. Perform.* **2021**, *30*, 5323–5332. [[CrossRef](#)]
36. Zheng, D.; Zhu, S.; Wang, F. The influence of TiAlN and enamel coatings on the corrosion behavior of Ti6Al4V alloy in the presence of solid NaCl deposit and water vapor at 450 °C. *Surf. Coat. Technol.* **2007**, *201*, 5859–5864. [[CrossRef](#)]
37. Kim, M.J.; Yadav, P.; Lee, D.B. Isothermal and Cyclic Oxidation of Ti-6Al-4V Alloy. *Defect Diffus. Forum* **2016**, *369*, 99–103. [[CrossRef](#)]
38. Ciszak, C.; Popa, I.; Brossard, J.-M.; Monceau, D.; Chevalier, S. NaCl induced corrosion of Ti-6Al-4V alloy at high temperature. *Corros. Sci.* **2016**, *110*, 91–104. [[CrossRef](#)]
39. Yang, Z.; Liang, W.; Miao, Q.; Chen, B.; Ding, Z.; Roy, N. Oxidation behavior of Al/Cr coating on Ti2AlNb alloy at 900 °C. *Mater. Res. Express* **2018**, *5*, 046408. [[CrossRef](#)]
40. Xiong, Y.; Zhu, S.; Wang, F. Synergistic corrosion behavior of coated Ti60 alloys with NaCl deposit in moist air at elevated temperature. *Corros. Sci.* **2008**, *50*, 15–22. [[CrossRef](#)]